DOI: 10.1002/chem.200601249

Current–Voltage Characteristics of a Homologous Series of Polycyclic Aromatic Hydrocarbons

Thilo Böhme,[a] Christopher D. Simpson,[b] Klaus Müllen,*[b] and Jürgen P. Rabe*[a]

Abstract: A novel alkyl-substituted polycyclic aromatic hydrocarbon (PAH) with D_{2h} symmetry and 78 carbon atoms in the aromatic core (C78) was synthesized, thereby completing a homologous series of soluble PAH compounds with increasing size of the aromatic π system (42, 60, and 78 carbon atoms). The optical band gaps were determined by UV/Vis and fluorescence spectroscopy in solution. Scanning tunneling microscopy (STM) and spectroscopy (STS) revealed diode-like current versus voltage (*I–V*) characteristics through individual aromatic cores in monolayers at the interface between the solution and the basal plane of graphite. The asymmetry of the current–voltage (*I–V*) characteristics increases with the increasing size of the aromatic core, and the concomitantly decreasing HOMO–LUMO gap. This is attributed to resonant tunneling through the HOMO of the adsorbed molecule, and an asymmetric position of the molecular species in the tunnel junction. Consistently, submolecularly resolved STM images at negative substrate bias are in good agreement with the calculated pattern for the electron densities of the HOMOs. The analysis provides the basis for tailoring rectification with a single molecule in an STM junction.

Keywords: cyclodehydrogenation · hydrocarbons · nanotechnology · polycycles · scanning tunneling microscopy

Introduction

The electronic properties of aromatic molecules at interfaces are of significant interest for new microelectronic and nanoscopic devices.[1] Already, single molecules between electrodes may perform basic functions of digital electronics, such as rectification, amplification, and switching.[2,3] Scanning tunneling microscopy (STM)[3–9] together with scanning tunneling spectroscopy (STS)[3,10,11] are powerful tools for structural and electronic characterization of single molecules in self-assembled monolayers on conducting substrates.

Alkylated hexa-*peri*-hexabenzocoronene (HBC; **1b**), consisting of 42 aromatic carbon atoms, and a related aromatic moiety with 60 carbon atoms (**2b**) are polycyclic aromatic hydrocarbon (PAH) systems, which may be considered as a nanoscale oligomeric version of an infinite graphene. Monolayers of these have been investigated by STM,[3,6] and STS has been used to study the electronic properties of the alkylated HBC (**1b**) on the submolecular scale.[3] As the aliphatic parts exhibit symmetric *I–V* characteristics, an asymmetric, diode-like electrical behavior was observed for the aromatic cores, which can be explained by a resonant amplification of the tunneling current through the HOMO at negative sample bias. The electronic properties of large PAH systems like HBC are also reflected in thermotropic liquid-crystalline phases, in which the aromatic, disc-shaped molecules form columnar structures, which behave like discotic nanowires: they exhibit one-dimensional transport of charge carriers and excitons along the columns with high charge-carrier mobility.[12]

Homologous series, that is, series of structurally closely related compounds that differ only in certain discrete parameters like, for example, symmetry or the number of repeating units and, thus, the size of the system, provide an interesting opportunity to determine structure–property relationships. A textbook case is the series of acenes, from benzene to naphthalene up to pentacene.[13] In such a series the physical and chemical properties can be expected to change in a regular fashion with the size or the number of π electrons, respectively.[14]

[a] Dr. T. Böhme, Prof. Dr. J. P. Rabe
Department of Physics, Humboldt University Berlin
Newtonstr. 15, 12489 Berlin (Germany)
Fax: (+49) 30-2093-7632
E-mail: rabe@physik.hu-berlin.de

[b] Dr. C. D. Simpson, Prof. Dr. K. Müllen
Max Planck Institute for Polymer Research
Ackermannweg 10, 55128 Mainz (Germany)
Fax: (+49) 6131-379-350
E-mail: muellen@mpip-mainz.mpg.de

Here we present a tunneling spectroscopic investigation of the *I–V* characteristics through a homologous series of alkylated PAH systems with increasing aromatic core size. The molecules were immobilized by self-assembly at the interface between an organic solution and the basal plane of highly oriented pyrolytic graphite. They were first imaged by STM and then the individual *I–V* characteristic positions of the adsorbate layer defined above were recorded. This approach allows the combination of in-situ high-resolution structural and electronic investigations of aromatic molecules of a weakly interacting substrate.

Results and Discussion

Synthesis: The large PAH systems C42 (**1a**), C60 (**2a**), and C78 (**3a**; Scheme 1) represent a homologous series with the size systematically increasing by three benzene rings or 18

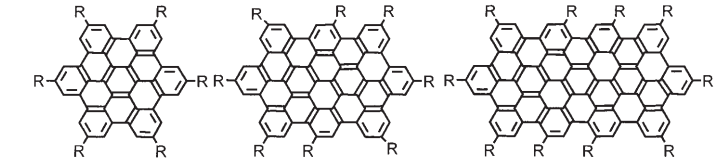

	C42	C60	C78
R = H	**1a**	**2a**	**3a**
R = $C_{12}H_{25}$	**1b**	**2b**	**3b**
E_g =	2.7 eV	2.3 eV	2.1 eV

Scheme 1. Chemical structures of the investigated homologous series and their respective HOMO–LUMO gaps.

carbon atoms in one direction of a molecular symmetry axis. Because the unsubstituted molecules are barely soluble in common organic solvents, solution-processable materials were targeted by alkyl-chain substitution of the aromatic cores. With the alkyl-substituted derivatives of C42 (**1b**) and C60 (**2b**) already at hand,[3,6] it became necessary to find a new synthetic pathway to an alkylated C78 PAH. The requirement was to find a way to attach as many alkyl chains as possible to the molecule for solubility reasons without them sterically interfering with each other and possibly hindering the final planarization step (see below). The solution turned out to be the procedure outlined in Scheme 2, based on our construction principle for PAH systems reported previously.[15] It leads to a C78 PAH (**3b**) substituted with ten alkyl chains that are arranged geometrically in an analogous way to the alkyl-substituted C60 unit (**2b**).

The initial step is the reaction of 1,4-dibromo-2,5-diiodobenzene with Grignard reagents to form iodo-functionalized *para*-terphenyl derivatives as reported by Hart and co-workers.[16] The reaction of **4** with *para*-dodecylphenylmagnesiumbromide followed by quenching with iodine afforded the terphenyl **5** in 46% yield. This yield was not very high; however, the starting material **4** could be partly regained as

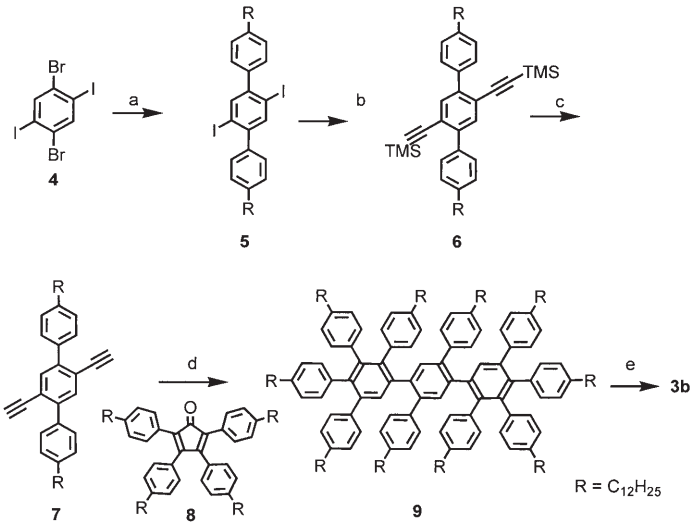

Scheme 2. Synthesis of the alkyl-substituted C78 PAH **3b**. Reagents, conditions and yields: a) $C_{12}H_{25}PhMgBr$, I_2, THF, 46%; b) TMSA, CuI, Pd[PPh_2]Cl_2, PPh_3, NEt_3, 76%; c) KF, H_2O, DMF, 90%; d) Ph_2O, 200°C, 90%; e) $FeCl_3$, CH_3NO_2, CH_2Cl_2, 83%.

a side product, improving the overall balance somewhat. In the next step, terphenyl **5** was treated with trimethylsilylacetylene in a palladium-catalyzed Hagihara–Sonogashira coupling to smoothly form the protected dialkyne **6** (76%).[17] The silyl groups were cleaved with potassium fluoride in DMF to yield **7** (90%). For the synthesis of the oligophenylene **9**, the unprotected dialkyne **7** was heated with two equivalents of the tetraphenylcyclopentadienone[8] (**8**) in diphenyl ether at 200°C overnight. The precursor molecule evolving carbon monoxide to afford the precursor molecule **9** in 90% yield.

The final cyclodehydrogenation step was the most critical one in the whole synthetic procedure. The conversion has to give high yields because there is not much hope of removing possible side products due to the expected comparatively low solubility of the target compound. The removal of 28 hydrogen atoms sets high demands on the efficiency of the individual aryl–aryl bond-formation step. For alkyl-substituted C42 PAH systems, iron(III) chloride, predissolved in nitromethane, injected into a solution of the precursor molecule in dichloromethane has proven to be the best method.[8] However, for the previous synthesis of octaalkyl C60 (**2b**), this method only yielded a partially cyclized product that had to be treated subsequently with potassium to afford the desired product.[6]

By increasing the reaction time and the excess of oxidizing agent per bond to be closed, conditions were found under which the C78 PAH (**3b**) was formed in high purity in a single cyclodehydrogenation step with iron(III) chloride. Analysis of the dark-red product relied strongly on isotopically resolved MALDI-TOF mass spectrometry, because although the compound turned out to be soluble enough for UV/Vis spectroscopy it was not soluble enough for solution NMR experiments.

Applying the newly found cyclodehydrogenation conditions to the C60 PAH (**2b**) again, it turned out that it too can be formed cleanly in one single reaction step, making it possible to obtain the compound without alkali-metal treatment in much higher quantities. The C60 (**2b**) was even soluble enough to be passed over silica gel with hot toluene and was then reprecipitated from chloroform. Structural proof was obtained by mass spectrometry and NMR spectroscopy.

UV/Vis and fluorescence spectroscopy: Due to their poor solubility in common solvents, UV/Vis spectra of the unsubstituted parent PAH systems C42, C60, and C78 (**1a**, **2a**, and **3a**) had to be measured in thin films on a quartz substrate.[18] Now, with the alkyl-substituted derivatives of all three molecules available, it became possible to perform UV/Vis measurements in solvents like chloroform and to compare the results with the solid-state method. This comparison also has important implications for other large PAH systems, for which no soluble derivatives yet exist. The UV/Vis spectra of the unsubstituted- and alkyl-substituted-PAH systems are depicted in Figure 1. As expected, the bands are shifted bathochromically with increasing size of the π system. The most intense bands, the so-called β bands, exhibit this feature especially clearly. For the same aromatic chromophore, the spectra of the substituted compounds in solution confirm the results of the solid-state method. The β bands remain at the same position within the error margin, whereas the overall spectrum is much better resolved and shows more detail.

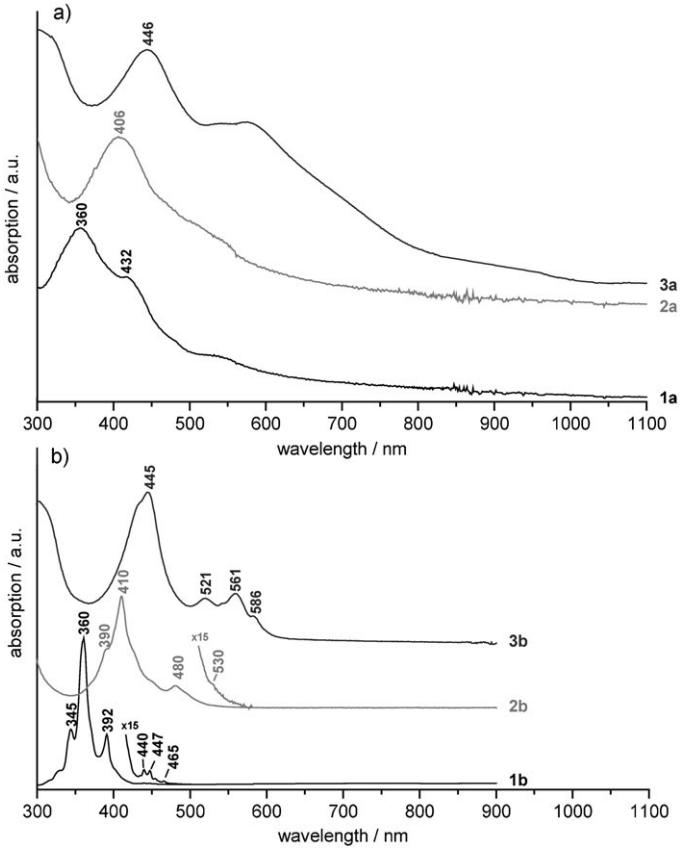

Figure 1. UV/Vis spectra of: a) the unsubstituted PAH systems **1a**, **2a**, and **3a** in thin films; b) the substituted PAH systems **1b**, **2b**, and **3b** in chloroform.

For each PAH molecule, the highest wavelength absorption peak (λ_{max}) reflects a transition from the lowest energy vibrational level in the ground state to the lowest energy vibrational level in the exited state and is a good estimate of the HOMO–LUMO energy gap. From the solid-state UV/Vis spectra, this value is almost impossible to determine because the bands are too broad and unresolved, hence the importance of well-resolved solution spectra. For the C42 and C60 molecules, the λ_{max} peaks have a very low relative intensity so that their spectra, shown in Figure 1, need to be enlarged in the corresponding area to identify the values of 465 nm (2.7 eV)[20] and 530 nm (2.3 eV), respectively. Excitation and fluorescence spectra serve as a further confirmation, because the transitions exhibit different relative intensities, as shown in Figure 2, for the C60 PAH **2b**. In the UV/Vis spectrum of the C78 PAH **3b**, the λ_{max} peak has a much higher relative intensity and can be identified directly as 586 nm (2.1 eV). These values serve as a reference for the discussion of the STS data presented below.

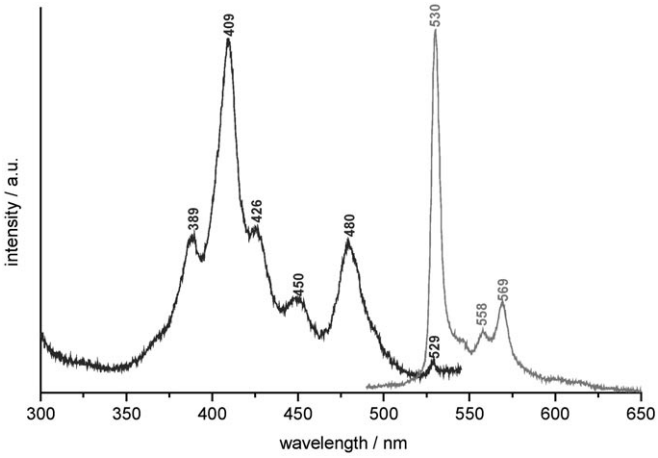

Figure 2. Excitation and fluorescence spectra of octaalkyl C60 (**2b**) in chloroform ($\lambda_{ex}=569$ nm, $\lambda_{em}=480$ nm).

Scanning tunneling microscopy: The self-assembly of alkylated C42 (**1b**) and C60 (**2b**) was previously studied by STM,[3,7] whereas C78 (**3b**) is investigated here for the first time. Figure 3 displays STM current images of C78 (**3b**) self-assembled at the interface between a solution in trichlorobenzene and the basal plane of graphite. The positions of the aromatic cores are assigned to areas of high tunneling currents (appearing bright), whereas the darker parts are attributed to the alkyl side chains giving rise to a lower tunneling probability.[5] In addition, there is submolecular detail in the aromatic regions, whereas due to their higher segmental mobility, the long alkyl chains are not resolved.

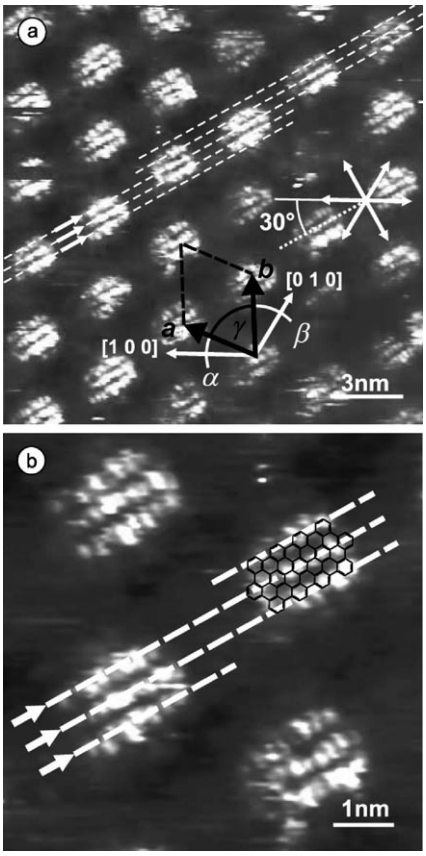

Figure 3. STM current images (constant-height mode) with two different tips of a monolayer of **3b** with submolecular resolution showing distinctive patterns in the aromatic region of the molecules. Sample bias: −0.7 V; Current setpoint: 200 pA; Scan rate: 976 nm s^{-1}.

The ordered molecular structure is characterized by its unit cell ($|a|=3.23\pm0.05$ nm, $|b|=3.4\pm0.1$ nm, $\gamma=66\pm3°$, $A=10.0\pm0.4$ nm^2, with one molecule per unit cell); the angle between the unit cell vector *a* and the [1 0 0] direction of the substrate ($32\pm3°$); and the orientation of the molecule within the unit cell. This implies that the aromatic core of the C78 molecule is oriented like an additional graphite segment, similar to a different PAH derivative investigated before.[8] Necessarily, the observed molecular orientation results in a 30° angle between the long molecular axis and a crystallographic axis of the graphite lattice (zig-zag row in graphite). Because the exact binding site of the molecule cannot be determined from the STM images, we expect a registry with graphite complying with an α–β stacking with respect to the uppermost substrate layer. The spatial requirement for a single molecule lying flat on a surface (footprint) is 10.0 nm^2, given by its van der Waals circumference.[21] The spatial requirement for the molecule is in excellent agreement with the provided space per unit cell, indicating a tight molecular packing in the adsorbate layer with no protrusion of alkyl side chains into the supernatant solution.

The submolecular image contrast exhibits additional patterns in the aromatic region, consisting of bright spots lined up in three rows parallel to the long molecular axis, partly smeared out to stripes. The measured distance between two adjacent rows amounts to about 0.4–0.5 nm as indicated in Figure 3. Three stripes with the same orientation and comparable spacing had previously been observed in the aromatic region for the C60 system **2b**.[6] Hence, the observed pattern can be regarded as a characteristic feature for this class of molecules.

The frontier orbitals of a free molecule **3a** were calculated by using a semiempirical method[22] (Figure 4). The tunneling current distribution in the aromatic region of **3b** (Figure 3b) resembled the square of the calculated wave function of the HOMO of the free molecule, indicating a correlation between a high electron density in the HOMO and the positions of an increased tunneling probability in the STM image. It also supports the hypothesis of a resonant increase of the tunneling probability by the HOMO. Moreover, a similarity with the LUMO wave function is not recognized, because, for example, the number of stripes in the STM image and the calculation do not agree. Instead of three, the LUMO wave function exhibits seven lobes running parallel to the long molecular axis (Figure 4).

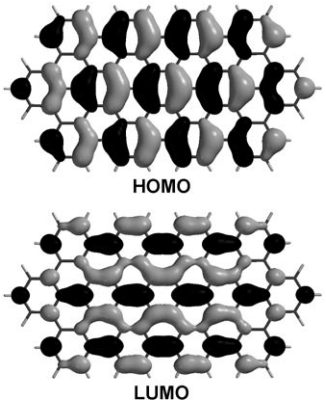

Figure 4. Wave functions of the frontier orbitals of a C78 PAH (**3a**) calculated with AM1[22]. Grey and black denote the sign of the wave function.

Upon comparing the distance between adjacent stripes in the STM image with the theoretical value according to the HOMO wave function, we noticed that the theoretically expected distance amounts to 0.37 nm, which means a small, but not negligible, difference between the experimental and the theoretical values. It possibly reflects the influence of the underlying graphite substrate, because it is known that the molecular STM contrast depends also on the adsorption site on the substrate and can change with different positions of the molecule.[4c,6] Furthermore, the adsorbed molecule can induce perturbations in the surface charge density of the substrate which finally is resolved in the STM experiment.[23] From this point of view, the observed patterns in the aromatic regions of **3b** could also be ascribed to an electronic superstructure within graphite caused by the adsorbed molecule. Incidentally, the distance between second-neighbor

armchair rows of the substrate lattice, which are oriented along the direction of the long molecular axis, is 0.49 nm, which also fits to the observed stripes.

Scanning tunneling spectroscopy (STS): Figure 5 presents the original data set of the *I–V* characteristics recorded above the aromatic parts of C42 (**1b**), C60 (**2b**), and C78

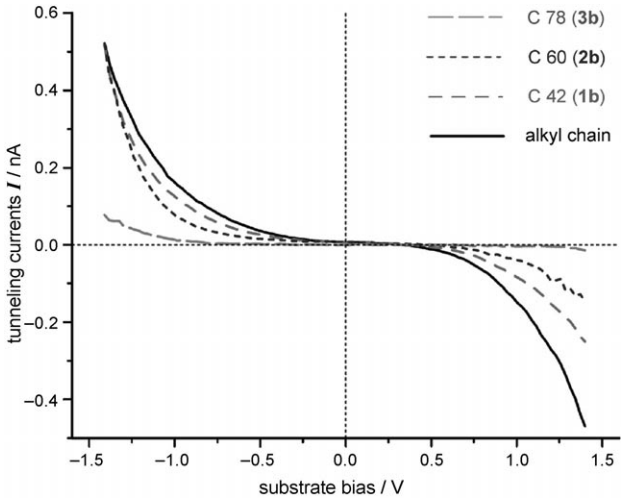

Figure 5. Original data set: $I(U)$ curves recorded at fixed tip-to-substrate distances. Distances adjusted according to substrate bias −1.4 V, setpoint 0.5 nA (alkyl chains, C42, C60) and 0.08 nA (C78). Bias ramp from −1.4 to +1.4 V.

(**3b**). The bias range is limited by the stability of the molecular layer at the interface between the rather inert graphite and the organic solution, indicative of electrochemical reactions at higher biases. As a consequence, only the onset of oxidation and reduction peaks can be observed. The alkyl moiety was probed spectroscopically in the same experiment together with the C42 aromatic core. All plotted *I–V* characteristics were averaged over several separate measurements. The characteristic for the aliphatic part exhibits a rather symmetric behavior with respect to the point of origin, which resembles the spectrum of the pure graphite substrate.[3,24] A small residual asymmetry is attributed to the different electrodes, that is, the Pt/Ir tip and graphite substrate. The *I–V* characteristics through the aromatic moieties, on the other hand, exhibit a clearly asymmetric, diode-like behavior.

The tip-to-substrate distance during the *I–V* data collection was fixed according to the sample bias of −1.4 V and the selected tunneling current setpoint of 0.5 nA (0.08 nA for C78). As the bias ramp also started at −1.4 V, the chosen setpoint was clearly reflected by the onset of each *I–V* characteristic. The tip-to-substrate distance is expected to be different for each presented *I–V* characteristic even with the same values for the bias voltage and current setpoint, due to the different electronic properties of the molecules resulting in different tunneling probabilities. These tip-to-substrate distances impinge on the tunneling spectra and have to be considered when comparing the *I–V* characteristics with each other. As pointed out earlier, the absolute tip-to-substrate distance is experimentally not accessible and remains unknown. Still, a correction for the different distances was performed based on the assumption that for a positive sample bias (and for the chosen experimental conditions) the *I–V* characteristics are dominated by the tunneling tip, the substrate and the tip-to-substrate distance, but not by the adsorbed molecules. This issue will be discussed in more detail below, after introducing a model, upon which the interpretation of the obtained *I–V* spectra is based.

The work function of graphite is about 4.7 eV,[25] and the ionization energy of aliphatic systems is about 10 eV (e.g., 9.6 eV for undecane),[26] indicating a large distance between the HOMO state and the Fermi edge of graphite when the molecule is adsorbed to the substrate. The σ–σ transitions in aliphatic structures like the peripheral alkyl groups of the investigated systems occur at wavelengths below 170 nm, corresponding to a large HOMO–LUMO gap of more than 7.3 eV. The adsorption process, however, involves electronic interactions at the interface. Because the mutual influence upon their electronic properties is not known in detail, a reasonable first-order approximation is a symmetric location of both HOMO and LUMO with respect to the Fermi level, with the HOMO–LUMO splitting of the adsorbed molecule being mainly unaffected upon adsorption. In this model the distance of the molecular frontier orbitals with respect to the Fermi level is about 3.5 eV. A direct coupling of these states during a spectroscopic scan of ±1.4 V to the tunneling current seems extremely unlikely. Even the assumption of a slightly asymmetric alignment does not change that picture in principle, because the frontier orbitals remain far away from the Fermi edge.

For the aromatic parts with its smaller HOMO–LUMO gap the situation is different. A value for the ionization energy is available for the parent compound **1a** only, namely 6.87 eV.[27] Taking this value into account, the difference in energy between HOMO and Fermi level of graphite (isolated systems) is about 2.2 eV. However, in analogy to the aliphatic case, this quantity does not reflect the energetic difference between HOMO and Fermi level in the joint system. Again, we consider the HOMO–LUMO splittings (Scheme 1), but assume here an asymmetric alignment of the frontier orbitals with the HOMO being closer to the Fermi level as proposed for electron-donating molecules.[11] In this picture, the distance between the HOMO of the C42 compound and the Fermi level of graphite becomes smaller than 1.35 eV. As the HOMO–LUMO gap decreases for the larger aromatic systems, the HOMO is expected to become closer to the Fermi level. This issue is illustrated in Figure 6.

Additionally, the asymmetric position of the adsorbate layer in the tunneling gap plays an important role. The layer of molecules is expected to be closer to the substrate than to the tip entailing an asymmetric current response of the system (see Figure 7c and d). Therefore, at negative sample bias we expect a distinct resonant contribution to the tunneling current for each investigated species except for the

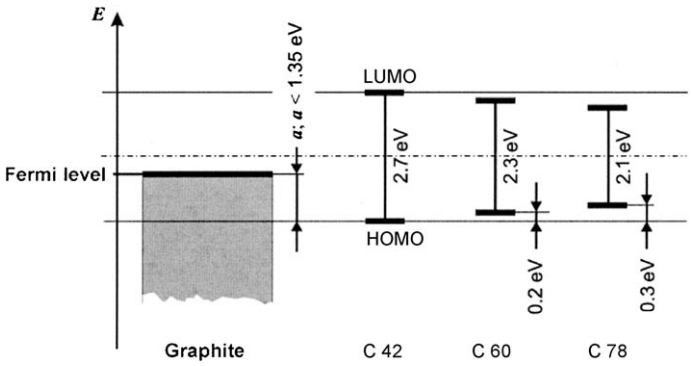

Figure 6. Schematic display of the asymmetric alignment of HOMO and LUMO of the individual molecule relative to the Fermi level of graphite with the HOMO being closer. We assume the HOMO–LUMO splitting of the free molecule to be mainly unaffected upon adsorption and the absolute position of the frontier orbitals with respect to the Fermi edge is not known. For simplicity the HOMO–LUMO gaps are arranged symmetrically to each other, resulting in a decreasing distance between HOMO and Fermi edge with increasing size.

aliphatic chains, whereas for a positive sample bias such a resonant amplification is not possible. Within the suggested model the tunneling current is even independent from the molecular species. Hence, we attribute the appearance of different tunneling currents at +1.4 V to different tip-to-sample distances. As explained earlier, these different distances originate from the particular experiment as the actual tip-to-substrate distance is adjusted for each molecular system according to the tunneling probability at −1.4 V. The intention for normalizing the currents at +1.4 V is to mimic the same tip-to-substrate distance for all molecular systems, taking the alkyl chain data as calibration reference. Each of the averaged *I–V* characteristics was multiplied by a constant factor so that the same current at +1.4 V was obtained. The resulting normalized plots are shown in Figure 8. Starting from +1.4 V all the curves fall in line and split up at the negative side of the bias ramp at distinctive

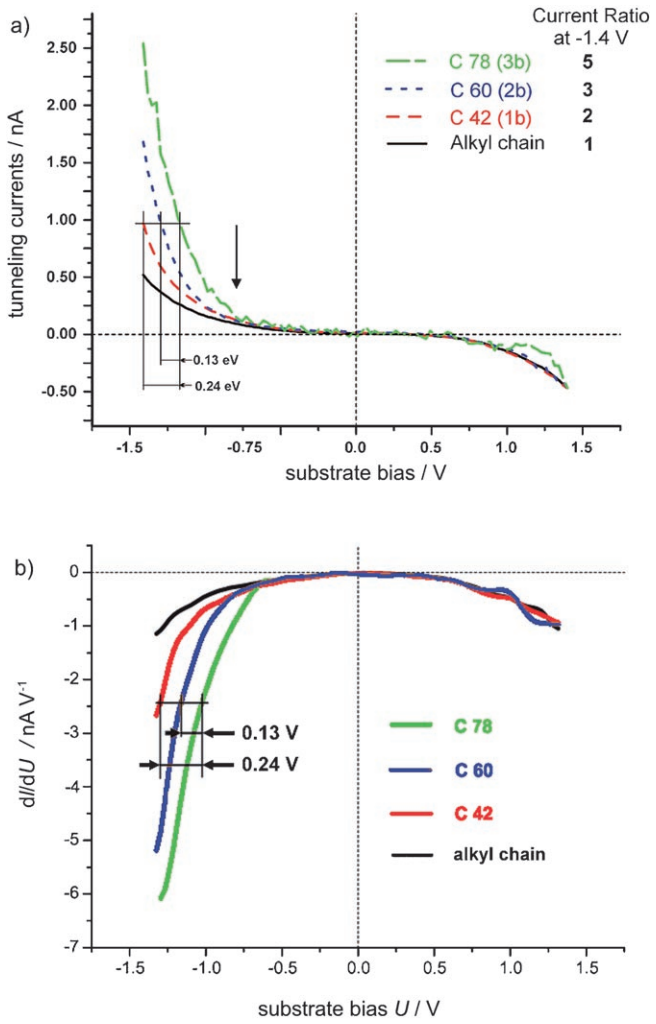

Figure 8. a) Normalized data set and b) derivatives of normalized data set.

voltages. Finally they approach similar slopes and go parallel. Compared to the normalized curve of C78 (**3b**) the others are shifted to higher negative voltages. The observation, that the curves exhibit a near-identical behavior for the complete positive side of the bias ramp can be regarded as support for the assumption that for a positive bias the *I–V* characteristics are independent of the adsorbed molecule.

We attribute the increase in the tunneling current from a certain negative bias value onward to the onset of a resonant amplification. This occurs when the HOMO has reached the Fermi level of the STM tip, thus opening an additional tunneling channel through the

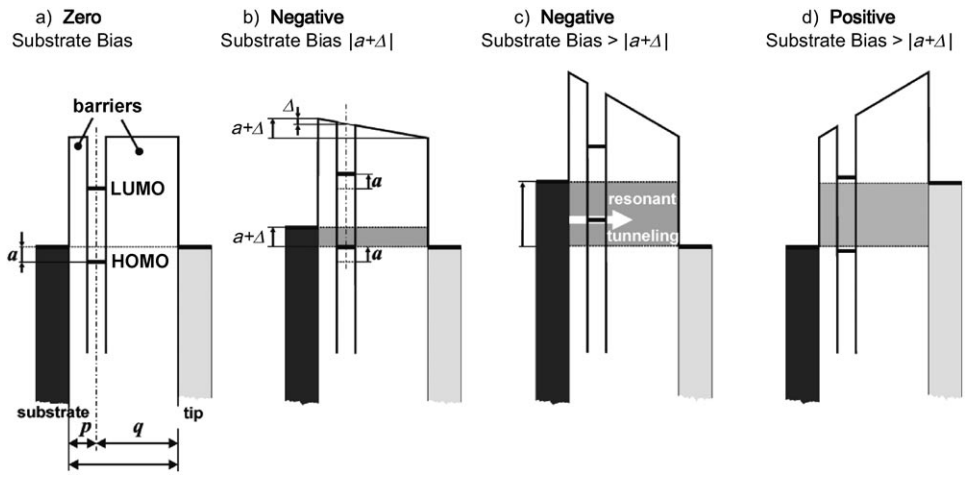

Figure 7. Resonant tunneling through a single molecule in a tunneling junction, explaining diode-like *I–V* characteristics.

HOMO. The resonance effect sets in first for the C78 (**3b**) compound, as for this system the energetic difference between HOMO and Fermi level is the smallest, followed by C60 (**2b**) and C42 (**1b**). In agreement with the applied model, there is no resonant amplification for the aliphatic moiety. Here, the *I–V* data basically reflects tip and substrate properties.

For C78 (**3b**) the threshold voltage $V_{Threshold}$ for resonant tunneling at which a noticeable increase in the tunneling current occurs was determined from the normalized *I–V* plot (Figure 8a) to be about −0.75 V. Compared to C78 (**3b**), the onset of resonance for the other aromatic compounds is not as clearly determined. To better determine these threshold voltages, the derivatives d*I*/d*V* (*V*) were calculated (Figure 8b). It can be observed that the slopes of the *I–V* characteristics increase continuously with negative bias values without approaching a constant value. With respect to the derivative of C78, the curves for the C60 and C42 compound reach the same d*I*/d*V* value at increasingly negative voltages. These voltage shifts, 0.14 and 0.28 V, are used for estimating the resonance thresholds for C60 and C42 to be about −0.9 and −1.0 V, respectively.

Even though these values reflect the proposed arrangement of the HOMOs introduced in Figure 6, the threshold voltage for resonant tunneling cannot directly be taken as equivalent for the energetic distance *a* between HOMO and Fermi level (compare with Figure 7a and b). In general, within the suggested model, *a* should be smaller than the value $eV_{Threshold}$. The reason is the quantity Δ, which is determined by the position of the molecule in the tunnel gap.[28] It is expected that with different tip-to-substrate distances the value of Δ changes slightly and therefore also the required bias to raise the HOMO of the adsorbed molecule to the Fermi level of the STM tip. This behavior could be of particular interest for the development of molecular electronics, as different *I–V* characteristics may be engineered from the same molecular species just depending on its position within a tunnel junction. However, further tunneling spectroscopic experiments have to be carried out in order to investigate this proposed behavior in more detail.

According to the introduced model (Figure 7), resonant contributions to the tunneling current are not limited to negative bias values. The fact that no resonance effects were observed for positive voltages can be taken as evidence for the asymmetric alignment of the molecule in the tunnel gap with a closer distance to the substrate. With a symmetric position, according to our model, an increase in resonance should be possible for both polarities at the same bias value giving rise to a symmetric current response. However, resonant tunneling may theoretically also be achieved with higher positive voltages than 1.4 V. This would include the possibility of resonant tunneling through the LUMO as well.

If the aromatic moiety were chemisorbed to the graphite surface instead of being physisorbed, the original molecular states would be fixed at the substrate and the quantity Δ would be equal to zero. The obtained *I–V* spectra may also be explained by using this concept. The threshold bias for resonant tunneling for C42 is 1.0 V, indicating an energy distance between HOMO and Fermi edge of ≤ 1 eV. According to the ionization energies of the isolated systems, the difference amounts to 2.2 eV. Hence, the HOMO state was raised upon adsorption by approximately 1.2 eV, which can be considered as evidence for a strong electronic interaction between substrate and adsorbate.

In the aromatic region of **3b**, additional patterns were observed, as described above. According to the *I–V* data, the threshold for the resonant amplification is −0.75 V. However, the bias setting for the presented highly resolved STM image (Figure 3) was −0.7 V. Other STM images (not shown here), which also clearly show three stripes above the aromatic parts of the C78 compound were recorded at −0.6 V. Furthermore, three stripes were already observed for C60,[6] for which the bias was also set to −0.6 V, whereas the threshold for resonance, derived from the tunneling spectroscopic measurements, was −0.9 V in this case. Thus, besides the resonant tunneling, there is probably a contrast contribution due to a convolution of the electronic properties of both substrate and adsorbate.

Conclusion

By improving the methods for oxidative cyclodehydrogenation of oligophenylenes, we succeeded in completing a homologous series of soluble, large PAH systems, with dimensions well into the nanometer scale and a HOMO–LUMO gap decreasing with molecular size. This represents a significant advance in the development of "superbenzene" chemistry based on HBC as modulus. Submolecularly resolved STM imaging and spectroscopy of the aromatic cores at solid–liquid interfaces revealed diode-like *I–V* characteristics, the asymmetry of which increases as the HOMO–LUMO gap decreases with molecular size. The analysis on the basis of a resonant tunneling model provides the basis for the development of tailor-made molecular electronic devices. In particular, the rectification should be improved as the aromatic core increases and the HOMO–LUMO gap decreases accordingly. However, the improvement will be limited for the currently accessible polycyclic hydrocarbons. Alternatively, strong donors and acceptors should allow the fabrication of diodes with even more pronounced rectification properties.

Experimental Section

^{1}H and ^{13}C NMR were recorded in $CDCl_3$, $CDCl_3/CS_2$ (1:1), and CD_2Cl_2 on Bruker DPX 250, Bruker 300 AMX, and Bruker 500 DRX instruments with use of the solvent proton or carbon signals as internal standard. Melting points were determined on a Büchi hot-stage apparatus and are uncorrected. Mass spectra were obtained by using a VG Instruments ZAB 2-SE-FPD by using FD. Elemental analysis was carried out by using a Foss–Heraeus Vario EL instrument in the Institute for Organic Chemistry at the Johannes Gutenberg University, Mainz. Diphenyl ether (99%), triphenylphosphane (97%), nitromethane (96+%), (all from Al-

drich) were used as received. Iron(III) chloride (98%), triethylamine (99%), and copper iodide (98%) (all from Merck) were used as received. Bis(triphenylphosphane)palladium(II)dichloride (99%), (from Strem) was used as received. Methanol, ethanol, toluene, dichloromethane, and chloroform (A.C.S. reagent, Riedel-de Haën) were used as received.

Octadodecyl-C60 (2b): 4′,5′,6′,3″,4″,5″-Hexakis-(4-dodecylphenyl)-1,1′:2′,1″:2″,1‴-quaterphenyl (440 mg, 0.209 mmol) was dissolved in dichloromethane (70 mL). A weak stream of argon was bubbled through the solution. Dry iron(III) chloride (1.0 g, 6.26 mmol) was dissolved in nitromethane (8 mL) and was added within 2 min. After 3 h, ethanol was added and the resulting precipitate filtered. The precipitate was filtered over a short pad of silica gel with hot toluene and was finally recrystallized from chloroform to yield **2** (270 mg, 60%) as a bright-orange solid. ^{1}H NMR (500 MHz, *p*-dichlorobenzene, 160°C): $\delta = 9.51$ (s, 2H), 9.28 (s, 2H), 9.21 (s, 8H), 9.15 (s, 2H), 4.21 (m, 4H), 3.66 (m, 12H), 2.65 (m, 4H), 2.55 (m, 12H), 2.2–1.4 (m, 144H), 1.12 ppm (t, ^3J(H,H) = 6.4 Hz, 24H); ^{13}C NMR (125 MHz, CS_2/$CDCl_3$, 40°C): $\delta = 139.3$, 139.2, 137.5, 135.7, 129.6, 129.4, 129.2, 128.7, 128.6, 126.2, 125.5, 123.9, 123.4, 123.2, 122.8, 122.3, 120.8, 120.6, 120.3, 118.7, 118.6, 118.3, 38.5, 37.6, 37.4, 32.9, 32.7, 32.6, 32.1, 30.8, 30.4, 30.3, 30.2, 30.1, 30.1, 30.0, 29.9, 29.9, 29.6, 22.9, 14.2 ppm; UV: λ_{max} (ε) = 289 (43), 391 (36), 410 (69), 480 nm (14×10^3 L mol^{-1} cm^{-1}); MALDI-TOF MS: *m*/*z* (%): 2088.0 (58), 2088.8 (87), 2089.9 (100), 2090.9 (61), 2092.0 (23), 2092.8 (11); elemental analysis calcd (%) for $C_{156}H_{214}$: C 89.68, H 10.32; found: C 89.67, H 10.36.

4,4″-Didodecyl-2′,5′-diiodine-*p*-terphenyl (5): A solution of compound **4** (3.0 g, 6.15 mmol) in dry THF (25 mL) was slowly added over 30 min to a solution of 4-dodecylphenylmagnesiumbromide (30.8 mmol) in THF (100 mL). The reaction mixture was stirred for 2 h, then it was cooled to 10°C and iodine (6.27 g, 24.60 mmol) was added. After further stirring for 1 h at 10°C the reaction was quenched by addition of ice water, and the mixture was extracted with dichloromethane. Subsequently the organic phase was dried over magnesium sulfate. After evaporating the solvent, the residue was washed with toluene and purified by column chromatography on silica gel with petroleum ether/dichloromethane (5:1) to afford **5** (2.3 g, 46%) as a colorless solid. M.p. 97°C; ^{1}H NMR (300 MHz, CD_2Cl_2): $\delta = 7.86$ (s, 2H), 7.27 (m, 8H), 2.67 (t, ^3J(H,H) = 7.6 Hz, 4H), 1.7–1.2 (m, 40H), 0.88 ppm (t, ^3J(H,H) = 6.9 Hz, 6H); ^{13}C NMR (75 MHz, CD_2Cl_2): $\delta = 145.8$, 142.0, 139.6, 138.6, 127.9, 126.9, 34.6, 30.8, 30.3, 28.6, 28.5, 28.4, 28.3, 21.6, 12.8 ppm; FD MS: *m*/*z* (%): 818.4 (100) [M^+]; elemental analysis calcd (%) for $C_{42}H_{60}I_2$: C 61.61, H 7.39; found: C 60.94, H 7.09.

4,4″-Didodecyl-2′,5′-di(trimethylsilylethinyl)-*p*-terphenyl (6): Compound **5** (2.3 g, 2.8 mmol), copper(I) iodide (0.11 g, 0.58 mmol), triphenylphosphane (0.15 g, 0.58 mmol), and bis(triphenylphosphane)palladium(II)dichloride (0.20 g, 0.28 mmol) were dissolved under inert atmosphere in triethylamine (70 mL). Trimethylsilylacetylene (0.82 g, 8.4 mmol) was added and the reaction mixture was stirred overnight at 50°C. After cooling, the solution was poured into dichloromethane (200 mL) and hydrochloric acid (150 mL, 6 M). The organic phase was separated, washed with saturated ammonium chloride solution and water, and dried over magnesium sulfate. After evaporating the solvent, the crude product was purified by using column chromatography on silica gel with petroleum ether/dichloromethane (10:1) to afford **6** (1.6 g, 76%) as a pale-yellow oil. ^{1}H NMR (300 MHz, CD_2Cl_2): $\delta = 7.57$ (m, 6H), 7.25 (d, ^3J(H,H) = 7.8 Hz, 4H), 2.67 (t, ^3J(H,H) = 7.6 Hz, 4H), 1.7–1.2 (m, 40H), 0.88 (t, ^3J(H,H) = 6.9 Hz, 6H), 0.15 ppm (s, 18H); ^{13}C NMR (75 MHz, CD_2Cl_2): $\delta = 143.5$, 143.0, 137.0, 134.8, 129.7, 128.7, 122.3, 105.0, 100.0, 36.3, 32.6, 32.2, 30.4, 30.3, 30.2, 30.1, 30.0, 23.4, 14.4, 0.0 ppm; FD MS: *m*/*z* (%): 759.1 (100) [M^+].

4,4″-Didodecyl-2′,5′-diethinyl-*p*-terphenyl (7): KF (0.49 g, 8.45 mmol) in H_20 (2.5 mL) was added to Compound **6** (1.6 g, 2.10 mmol) dissolved in a mixture of DMF (40 mL) and THF (40 mL), under an argon atmosphere. After 3 h the reaction mixture was poured into water and was extracted with toluene; the organic phase was then dried with magnesium sulfate. After evaporating the solvent, the crude product was purified by using column chromatography on silica gel with petroleum ether/dichloromethane (5:1) to afford **7** (1.2 g, 90%) as a pale-yellow solid. M.p. 88°C; ^{1}H NMR (300 MHz, CD_2Cl_2): $\delta = 7.63$ (s, 2H), 7.54 (d, ^3J(H,H) = 8.4 Hz), 7.27 (d, ^3J(H,H) = 8.4 Hz), 3.21 (s, 2H), 2.67 (t, ^3J(H,H) = 7.6 Hz, 4H), 1.7–1.2 (m, 40H), 0.88 ppm (t, ^3J(H,H) = 6.9 Hz, 6H); ^{13}C NMR (75 MHz, CD_2Cl_2): $\delta = 143.5$, 143.1, 136.6, 135.3, 129.4, 128.6, 121.4, 83.1, 82.0, 36.1, 32.4, 31.9, 30.1, 30.0, 29.9, 29.8, 29.7, 23.1, 14.3 ppm; FD MS: *m*/*z* (%): 614.9 (100) [M^+]; elemental analysis calcd (%) for $C_{46}H_{62}$: C 89.84, H 10.16; found: C 89.77, H 10.09.

4′,5′,6′,2″,5″,3‴,4‴,5‴-Octakis-(4-dodecylphenyl)-1,1′:2′,1″:4″,1‴:2‴,1⁗-quinquephenylene (9): Compounds **7** (1.1 g, 1.79 mmol) and **8** (3.79 g, 3.58 mmol) were heated overnight in diphenyl ether (30 mL) at 200°C. After cooling to RT ethanol (100 mL) was added to the reaction mixture. The solvent was decanted and the residual oil was purified by column chromatography on silica gel with petroleum ether/dichloromethane (10:1) to afford **9** (4.5 g, 94%) as a colorless solid. M.p. 69°C; ^{1}H NMR (500 MHz, $C_2D_2Cl_4$): $\delta = 7.5$–6.3 (m, 22H), 2.6–2.1 (m, 20H), 1.6–1.0 (m, 200H), 0.8 ppm (m, 30H); ^{13}C NMR (125 MHz, $C_2D_2Cl_4$): $\delta = 141.9$, 140.8, 140.4, 140.2, 139.9, 139.6, 139.5, 139.1, 138.5, 138.4, 138.1, 133.3, 132.8, 131.8, 131.6, 130.1, 129.8, 127.7, 127.5, 126.8, 126.5, 35.7, 35.6, 35.6, 32.2, 31.9, 31.4, 30.0, 29.9, 29.8, 29.6, 29.5, 29.1, 22.9, 14.3 ppm; FD MS: *m*/*z* (%): 2674.1 (100) [M^+]; elemental analysis calcd (%) for $C_{198}H_{294}$: C 88.92, H 11.08; found: C 88.87, H 11.04.

Decadodecyl-C78 (3b): Compound **9** (400 mg, 0.15 mmol) was dissolved in dichloromethane (70 mL). A weak stream of argon was bubbled through the solution. Dry iron(III) chloride (2.0 g, 12.5 mmol) was dissolved in nitromethane (15 mL) and was added over a period of 2 min. After 4 h, ethanol was added and the resulting precipitate was filtered, washed repeatedly with ethanol, and dried to yield **3b** (330 mg, 83%) as a dark-red solid. UV: λ_{max} (ε) = 304 (20), 446 (22), 521 (7), 561 (7), 586 nm (4×10^3 L mol^{-1} cm^{-1}); MALDI-TOF MS: *m*/*z* (%): 2643.5 (52), 2644.6 (100), 2645.7 (94), 2646.6 (72), 2647.6 (43), 2648.5 (16), 2649.6 (7); elemental analysis calcd (%) for $C_{198}H_{266}$: C 89.87, H 10.13; found: C 88.27, H 9.86.

Scanning tunneling microscopy and scanning tunneling spectroscopy (STM/STS): The STM and STS measurements were carried out under ambient conditions in situ at the solid–liquid interface between the basal plane of highly oriented pyrolytic graphite (HOPG) and 1,2,4-trichlorobenzene. We used a home-built beetle-type[28] low-current STM interfaced to Omicron electronics (Omicron Vakuumphysik GmbH, Germany). All experiments were carried out with mechanically cut Pt/Ir(80:20) tips. Graphite was cleaved in air. Samples were prepared by applying a drop of a nearly saturated solution of the sample to the STM junction. If the monolayer crystallization did not occur spontaneously it was induced by bias pulses of a few volts. When scanning and imaging the adsorbate layer the tunneling parameters *I* and *U* determined the tip-to-substrate distance the exact value of which is not well known. For the STS measurement the STM tip was moved to the position of interest with the feedback still activated. Therefore, the tip-to-substrate distance was adjusted according to the selected bias voltage and the setpoint for the tunneling current, before the feedback loop was interrupted. The vertical and lateral position of the tip was kept fixed, whereas a bias ramp from −1.4 to +1.4 V was swept through and the tunneling current recorded. The specified polarity refers to the sample. Imaging of the molecular systems beforehand was carried out at a sample bias of −1.4 V, even though this was not the optimal value for the image contrast for all the compounds. The main intention was to keep as many parameters as possible constant within the experiment in order to facilitate the analysis of the spectroscopic $I(U)$ data. The selected current setpoint for the **3b** was 0.08 nA, for all the other systems it was 0.5 nA. $I(U)$ data were only used if the STM images were stable and basically identical before and after the STS measurements. Many (between 4 and 54) separate measurements were recorded and averaged.

STM images of **3b** are presented without filtering. Fast Fourier transform (FFT) baseddigital-image processing (scanning probe image processor (SPIP), Image Metrology ApS) was performed in order to correct the images for distortion and drift, which was necessary for a precise characterization of the observed highly ordered structures and contrast features. The graphite lattice served as internal calibration standard. To resolve graphite before and/or after an image of the adsorbate layer was record-

ed, the tunneling parameters U and I were set to −0.1 V (sample bias) and 0.2 nA.

Acknowledgements

We wish to thank Dr. Jochen Beier for help with the fluorescence spectroscopy. This work was supported by the EU-TMR project SISITOMAS, the Volkswagen-Stiftung (Elektronentransport durch konjugierte molekulare Scheiben und Ketten) and the German "Bundesministerium für Forschung und Technologie" as part of the program "Zentrum für multifunktionelle Werkstoffe und miniaturisierte Funktionseinheiten" (BMBF 03N6500).

[1] C. Joachim, J. K. Gimzewski, A. Aviram, *Nature* **2000**, *408*, 541–548; A. Nitzan, M. A. Ratner, *Science* **2003**, *300*, 1384–1389.
[2] A. S. Martin, J. R. Sambles, G. J. Ashwell, *Phys. Rev. Lett.* **1993**, *70*, 218–221; C. Joachim, J. K. Gimzewski, *Chem. Phys. Lett.* **1997**, *265*, 353–357; S. J. Tans, A. R. M. Verschueren, C. Dekker, *Nature* **1998**, *393*, 49–52; R. M. Metzger, *Acc. Chem. Res.* **1999**, *32*, 950–957; Y. Wada, *Pure Appl. Chem.* **1999**, *71*, 2055–2066; H. Park, J. Park, A. K L. Lim, E. H. Anderson, A. P. Alivisatos, P. L. McEuen *Nature* **2000**, *407*, 57–60; W. Liang, M. P. Shores, M. Bockrath, J. R. Long, H. Park, *Nature* **2002**, *417*, 725–729; J. A. Misewich, R. Martel, P. Avouris, J. C. Tsang, S. Heinze, J. Tersoff, *Science* **2003**, *300*, 783–786; F. Jäckel, M. D. Watson, K. Müllen, J. P. Rabe, *Phys. Rev. Lett.* **2004**, *92*, 188303.
[3] A. Stabel, P. Herwig, K. Müllen, J. P. Rabe, *Angew. Chem.* **1995**, *107*, 1768–1770; *Angew. Chem. Int. Ed. Engl.* **1995**, *34*, 1609–1611; F. Jäckel, Z. Wang, M. D. Watson, K. Müllen, J. P. Rabe, *Chem. Phys. Lett.* **2004**, *387*, 372–376.
[4] a) G. Binnig, H. Rohrer, *Helv. Phys. Acta* **1982**, *55*, 726–735; b) J. K. Spong, H. A. Mizes, L. J. Lacomb, M. M. Dovek, J. E. Frommer, J. S. Foster, *Nature* **1989**, *338*, 137–139; c) J. P. Rabe, S. Buchholz, *Science* **1991**, *253*, 424–427; d) D. M. Cyr, B. Venkataraman, G. W. Flynn, A. Black, G. M. Whitesides, *J. Phys. Chem.* **1996**, *100*, 13747–13759; e) C. L. Claypool, F. Faglioni, A. J. Matzger, W. A. Goddard, N. S. Lewis, *J. Phys. Chem. B* **1999**, *103*, 9690–9699.
[5] D. P. E. Smith, H. Horber, C. Gerber, G. Binnig, *Science* **1989**, *245*, 43–45; R. Lazzaroni, A. Calderone, J. L. Bredas, J. P. Rabe, *J. Chem. Phys.* **1997**, *107*, 99–105; P. Sautet, *Chem. Rev.* **1997**, *97*, 1097–1116.
[6] V. S. Iyer, K. Yoshimura, V. Enkelmann, R. Epsch, J. P. Rabe, K. Müllen, *Angew. Chem.* **1998**, *110*, 2843–2846; *Angew. Chem. Int. Ed.* **1998**, *37*, 2696–2699.
[7] S. Ito, M. Wehmeier, J. D. Brand, C. Kübel, R. Epsch, J. P. Rabe, K. Müllen, *Chem. Eur. J.* **2000**, *6*, 4327–4342.
[8] S. Ito, P. T. Herwig, T. Böhme, J. P. Rabe, W. Rettig, K. Müllen, *J. Am. Chem. Soc.* **2000**, *122*, 7698–7706.
[9] A. Miura, Z. Chen, H. Uji-i, S. De Feyter, M. Zdanowska, P. Jonkheim, A. P. H. J. Schenning, E. W. Meijer, F. Würthner, F. C. De Schryver, *J. Am. Chem. Soc.* **2003**, *125*, 14968–14969.
[10] N. D. Lang, *Phys. Rev. B* **1986**, *34*, 5947–5950; P. H. Lippel, R. J. Wilson, M. D. Miller, C. Wöll, S. Chiang, *Phys. Rev. Lett.* **1989**, *62*, 171–174; R. M. Tromp, *J. Phys. Condens. Matter* **1989**, *1*, 10211–10228; X. H. Qiu, C. Wang, Q. D. Zeng, B. Xu, S. X. Yin, H. N. Wang, S. D. Xu, C. L. Bai, *J. Am. Chem. Soc.* **2000**, *122*, 5550–5556; J. I. Pascual, J. Gomez-Herrero, C. Rogero, A. M. Baro, D. Sanchez-Portal, E. Artacho, P. Ordejon, J. M. Soler, *Chem. Phys. Lett.* **2000**, *321*, 78–82; A. Gesquière, M. M. S. Abdel-Mottaleb, S. De Feyter, F. C. De Schryver, F. Schoonbeek, J. van Esch, R. M. Kellog, B. L. Feringa, A. Calderone, R. Lazzaroni, J. L. Brédas, *Langmuir* **2000**, *16*, 10385–10391; T. Schmitz-Hübsch, F. Sellam, R. Staub, M. Törker, T. Fritz, C. Kübel, K. Müllen, K. Leo, *Surf. Sci.* **2000**, *445*, 358–367; M. Toerker, T. Fritz, H. Proehl, R. Gutierrez, F. Grossmann, R. Schmidt, *Phys. Rev. B* **2002**, *65*, 245422; M. D. Watson, F. Jäckel, N. Severin, J. P. Rabe, K. Müllen, *J. Am. Chem. Soc.* **2004** *126*, 1402–1407.
[11] R. Strohmaier, J. Petersen, B. Gompf, W. Eisenmenger, *Surf. Sci.* **1998**, *418*, 91–104.
[12] A. M. van de Craats, J. M. Warman, K. Müllen, Y. Geerts, J. D. Brand, *Adv. Mater.* **1998**, *10*, 36–38; L. Schmidt-Mende, A. Fechtenkötter, K. Müllen, E. Moons, R. H. Friend, J. D. MacKenzie, *Science* **2001**, *293*, 1119–1122.
[13] E. Clar, *Ber. Dtsch. Chem. Ges. B* **1936**, *69*, 607–614.
[14] M. Zander, *Polycyclische Aromaten-Kohlenwasserstoffe und Fullerene* Teubner, Stuttgart, **1995**.
[15] M. D. Watson, A. Fechtenkötter, K. Müllen, *Chem. Rev.* **2001**, *101*, 1267–1300.
[16] H. Hart, K. Harada, C. J. F. Du, *J. Org. Chem.* **1985**, *50*, 3104–3110.
[17] S. Takahashi, Y. Kuroyama, K. Sonogashira, N. Hagihara, *Synthesis* **1980**, 627–630.
[18] F. Dötz, J. D. Brand, S. Ito, L. Gherghel, K. Müllen, *J. Am. Chem. Soc.* **2000**, *122*, 7707–7717.
[19] E. Clar, *Polycyclic Hydrocarbons*, Springer, Berlin, Göttingen, Heidelberg, **1964**.
[20] W. Hendel, Z. H. Khan, W. Schmidt, *Tetrahedron* **1986**, *42*, 1127–1134.
[21] Determined by using the visualization facilities supplied by the Insight software (Molecular Simulations).
[22] AM1, PC SpartanPro 1.0.5, Wavefunction
[23] J. Xhie, K. Sattler, U. Muller, N. Venkateswaran, G. Raina, *Phys. Rev. B* **1991**, *43*, 8917–8923; H. A. Mizes, J. S. Foster, *Science* **1989**, *244*, 559–562.
[24] Z. Klusek, *Appl. Surf. Sci.* **1998**, *125*, 339–350.
[25] R. F. Willis, B. Feuerbacher, B. Fitton, *Phys. Rev. B* **1971**, *4*, 2441–2452.
[26] S. G. Lias, *Ion Cyclotron Reson. Spectrom.* **1982**, 409431.
[27] E. Clar, W. Schmidt, *Tetrahedron* **1978**, *34*, 3219–3224.
[28] W. Mizutani, M. Shigeno, K. Kajimura, M. Ono, *Ultramicroscopy* **1992**, *42*, 236–241.
[29] K. Besocke, *Surf. Sci.* **1987**, *181*, 145–153.

Received: August 31, 2006
Revised: February 15, 2006
Published online: June 20, 2007

